Proceedings of the 41st Israel Annual Conference on Aerospace Sciences, Tel Aviv, Israel (2001).

COMPUTATIONAL MECHANICS IN MODELING OF AIRDROP SYSTEMS

Tayfun E. Tezduyar*
Team for Advanced Flow Simulation and Modeling (T⋆AFSM)†
Mechanical Engineering and Materials Science
Rice University - MS 321, 6100 Main Street
Houston, TX 77005, USA

Abstract

This paper is a review of the recent advances in computational mechanics research of the Team for Advanced Flow Simulation and Modeling (T⋆AFSM) [http://www.mems.rice.edu/TAFSM/] targeting airdrop systems. The specific applications we are focusing on include aerodynamic interaction between a cargo aircraft and a paratrooper or payload separating from that aircraft; aerodynamics of a parachute crossing the unsteady wake of an aircraft; aerodynamic response of parachutes subjected to wind shear; aerodynamic interaction between multiple parachutes; and aerodynamics of various stages of the parachute systems used in deceleration, gliding and landing of the Crew Return Vehicle of the International Space Station. The methods developed by the T⋆AFSM to address these computational challenges include special numerical stabilization methods; Deforming-Spatial-Domain/Stabilized Space-Time formulation; Enhanced-Discretization Interface-Capturing Technique; advanced mesh update methods; Multi-Domain Method; iterative solution methods for large equation systems; and parallel and multi-platform computing strategies. The review of these methods here is supplemented by a number of numerical examples from parallel computation of complex, 3D flow problems in airdrop systems.

1. INTRODUCTION

Modeling of airdrop systems is one of the "Targeted Challenges" of the Team for Advanced Flow Simulation and Modeling (T⋆AFSM), which is headquartered at the Department of Mechanical Engineering and Materials Science, Rice University, Houston, Texas [http://www.mems.rice.edu/TAFSM/]. Other areas of computational mechanics where the T⋆AFSM expects to make an impact, and therefore identified as "Targeted Challenges", are unsteady flows with interfaces; fluid-object interactions; fluid-structure interactions; air circulation and contaminant dispersion; and aerodynamics and hydrodynamics of complex shapes. The methods developed by the T⋆AFSM to address these challenges include special numerical stabilization methods; Deforming-Spatial- Domain/Stabilized Space-Time (DSD/SST) formulation; Enhanced-Discretization Interface-Capturing Technique (EDICT); advanced mesh update methods; Shear-Slip Mesh Update Method; Multi-Domain Method (MDM); iterative solution methods for large equation systems; and parallel and multi-platform computing strategies. In this paper, we provide an overview of the recent advances in research activities of the T*AFSM addressing airdrop systems. This overview is based on a number of recent papers published by the T⋆AFSM on the subject of airdrop systems (see [1–5]).

T⋆AFSM projects addressing various problems in airdrop systems are carried as collaborative work with researchers from the US Army Natick Soldier Center and NASA Johnson Space Center. A number of Rice undergraduate and graduate students have been working on these projects, and cadets from the US Military Academy (West Point) have also been participating as summer interns. Joint projects with Natick Soldier Center include aerodynamic interaction between a cargo aircraft and a paratrooper or payload separating from that aircraft; aerodynamics of a parachute crossing the unsteady wake of an aircraft; aerodynamic response of parachutes subjected to wind shear; and aerodynamic interaction between multiple parachutes. Collaborations with the Johnson Space Center are on simulation of various stages of the parachute systems used in deceleration, gliding and landing of the Crew Return Vehicle of the International Space Station.

*James F. Barbour Professor in Engineering and Chairman (http://www.mems.rice.edu/tezduyar/)
†http://www.mems.rice.edu/TAFSM/

When a cargo aircraft with relatively new design is put into operation, the aerodynamic interaction between the aircraft and a paratrooper separating from that aircraft becomes a very relevant issue in terms of successful and effective deployment of paratroopers. In this simulation, we consider a single paratrooper exiting the aircraft. The purpose is to calculate the path of the paratrooper relative to the aircraft, after his exit from the aircraft but prior to the opening of the parachute, while being subjected to aerodynamical forces in addition to gravity. This simulation was first reported in [6]. An improved geometric model for the aircraft was reported in [7]. The computation with this improved model of the aircraft and a more realistic model of the paratrooper was reported in [4]. The simulation is based an solving the Navier-Stokes equations of incompressible flows for flow around both the aircraft and the paratrooper while their relative positions are changing, coupled with solving the equations of motion for the paratrooper. The Deforming-Spatial-Domain/Stabilized Space-Time (DSD/SST) formulation [8–10] is used for solving this problem where the spatial domain occupied by air is changing in time.

The DSD/SST formulation was developed as a general-purpose method for computation of flows with moving boundaries and interfaces, such as two-fluid flows and fluid-structure interactions. This method automatically takes into account the motion of the boundaries and interfaces. At each time step of a computation, the locations of the boundaries and interfaces are calculated as part of the overall solution. The stabilized space-time formulations were used earlier by other researchers to solve problems with fixed spatial domains (see for example [11]). The DSD/SST formulation is based on the Galerkin/Least-Squares (GLS) formulation [12]. The Streamline-Upwind/Petrov-Galerkin (SUPG) [13,14] and Pressure-Stabilizing/Petrov-Galerkin (PSPG) [8] formulations are the essential components of the GLS formulation. When these stabilized formulations are implemented with a sound understanding of their underlying concepts, flows at high Reynolds numbers can be computed without introducing excessive numerical dissipation, and equal-order interpolations functions for velocity and pressure can be used to simplify the implementation.

Another component of the DSD/SST formulation is an automatic mesh moving technique, which is used for updating the mesh as the spatial domain occupied by the fluid changes its shape every time step. This mesh moving method, first introduced in [15], is based on moving the nodal points as governed by the equations of linear elasticity. The motion of the internal nodes is determined by solving these additional equations, with the boundary conditions for these mesh motion equations specified in such a way that they match the normal velocity of the fluid at the fluid-structure interface. Reducing the frequency of remeshing is the most important consideration taken into account in the development of the mesh moving method. For additional details, see [15].

In a multi-aircraft paratrooper deployment, as a parachute deployed from an aircraft crosses during its descent the wake of the preceding aircraft, it might become subjected to strong, unsteady aerodynamical forces. Although normally the distance between the two aircraft is quite large compared to the length scales of the aircraft, it may not be large enough for the parachute to be spared from these wake effects. Fluid-structure interactions play a significant role in the aerodynamic and structural response of the parachute to the wake effects, and need to be accounted for in numerical prediction of the parachute behavior. In addition to the formidable task involved in solving an unsteady fluid-structure interaction problem, the need to accurately solve unsteady flows over long wake regions poses a substantial challenge. This challenge motivated the T$\star$AFSM to develop the Multi-Domain Method (MDM) [7] for the class of simulations requiring computation of the long-wake flows generated by a primary object and, sometimes, influence of this wake on a secondary object placed far downstream.

In the MDM, the problem domain is divided into a sequence of overlapping subdomains. The primary object is placed in the first subdomain, and the subsequent subdomains cover the long-wake regions and secondary objects. While the inflow boundary conditions for the first subdomain are derived from the free-stream conditions, the inflow conditions for each of the remaining subdomains is extracted from the subdomain preceding it.

In 3D applications of the MDM reported in [16–18], we tested this method by computing the flow around

a small wing placed in the wake of a larger wing; computation of the first and second phases of the Karman vortex street in the wake of a circular cylinder up to 300 diameters downstream; and preliminary computation of the aerodynamics of a rigid parachute crossing the wake of an aircraft. A more comprehensive study of a rigid parachute crossing an aircraft wake, together with the MDM developed for that purpose, was presented in [1]. Simulation of the fluid-structure interactions of a flexible parachute crossing an aircraft wake was presented in [2]

The technique used for simulation of the aerodynamics and fluid-structure interactions of the parachute functions rather independently from the computation of the long-wake flow data that it relies on using. The wake data may have been computed earlier for a different purpose, or may have just been computed based specifically on the conditions of the parachute problem we wish to simulate. In the extreme case, the wake data can be computed almost concurrently with the computation of the parachute problem, provided that the wake computation is at least one time step ahead of the parachute computation.

The parachute fluid-structure interactions are computed over a domain that moves with the payload and traverses the space also covered by the domain used for computation of the wake flow. Therefore the parachute domain functions as one of the subdomains of the MDM designed specifically for simulating the parachute fluid-structure interactions considered here. The boundary conditions for the parachute domain are extracted from the flow field computed over the wake domain, at locations corresponding to the positions of those boundaries in the wake domain.

The computation over the first domain, which contains the aircraft, is based on a general-purpose implementation of a semi- discrete stabilized finite element formulation. The computation over the wake domain, which contains no objects, is based on a special-purpose implementation that exploits the simplicity of the mesh to increase the computational speed. The computation over the last domain, which contains the parachute, is based on a general- purpose implementation of the DSD/SST formulation, taking into account the fluid-structure interactions.

The fluid dynamics part of the problem is governed by the Navier-Stokes equations of incompressible flows. The structural dynamics part is governed by the nonlinear membrane equations, taking into account large displacements and rotations, but assuming small strains, as well as the equations governing the mechanics of the parachute suspension lines.

The DSD/SST formulation is coupled to the finite element formulation used for solving the membrane equations governing the structural mechanics of the parachute canopy and the equations governing the mechanics of the suspension lines. These coupled formulations have recently been applied also to simulation of the fluid-structure interactions for a round parachute descending through a wake-free (or uniform) environment (see [19]) and for a gliding ram-air parachute (see [20]). Here they are used in a computational technique that serves as a component of the MDM that has been designed for simulation of the fluid-structure interactions of a parachute crossing an aircraft wake.

Simulation of airdrop systems in some cases may involve computation of the aerodynamic interactions between parachute canopies. Such interactions can occur between two separate parachutes when the two paratroopers (or payloads) come close to each other. They can also occur between the canopies of a cluster of parachutes used for a single payload. Our review here includes computational models for and results from this class simulations. This work was reported in [5], where interactions between the canopies are assumed to be purely aerodynamic, with fluid-structure interactions playing no role. For the two-parachute interactions, we investigate how the aerodynamic behavior depends on the distance of separation. For the clusters, we investigate how the aerodynamic behavior varies depending on the number and arrangement of canopies in a cluster.

Normally, the Space Shuttle will transport the crew to and from the Space Station. However, in some cases, it might be necessary to bring the crew back sooner than the time required to send the Shuttle up. In such cases, the crew will use the Crew Return Vehicle (CRV), which can quickly be launched from the Space Station and can re-enter the atmosphere. However, the CRV, which is small and of fixed configuration, will

only utilize a sequence of parachutes to first slow it down, then glide it to the landing area, and finally, land it softly. Different types of parachutes will be used to accomplish these goals, starting with round parachutes to slow the CRV down, and ending with a large-ram air parachute (parafoil) to glide and land it (see Figure 1). Using parafoils to glide and soft-land large objects like the CRV is a new concept, and it

Figure 1. Crew Return Vehicle and parafoil in a flight test.

is difficult to perform laboratory tests with parafoils of the sizes required to land such large objects. These parafoils can also be used for gliding and soft landing of other classes of large objects, such as food crates or ground vehicles needed in an area that is hard to reach by any means other than a parachute.

The parafoil will go through a number of opening stages, starting with the smallest size in the first stage, expanding to its full size in the subsequent stages, and reaching its final geometric shape in the last stage. Simulation of progressing through these stages involves a number of computational challenges, including time-dependent shape transformations and fluid-structure interactions. Although we addressed these types of challenges in the past in the context of other applications (see [21, 19]), here we focus on computation of the discrete stages of the parafoil, without taking into account the fluid-structure interactions. These computations were reported in [3].

It is assumed that the airspeed during different disreefing stages of the parafoil is not high enough for the compressibility effects to be significant. Consequently, we use the Navier-Stokes equations of incompressible flows as the governing equations for the airflow. These equations are solved with a semi-discrete finite element formulation, based on the SUPG and PSPG stabilizations.

Discretization of the problems addressed here results in large, coupled nonlinear equation systems that need to be solved at every time step. The coupling between the blocks of equations corresponding to the Navier-Stokes, mesh moving, and membrane equations are handled in an iterative fashion. At each nonlinear iteration, the vectors of unknowns associated with these three blocks of equations are updated individually, based on the Newton-Raphson method. While updating the vector of unknowns associated with one of the blocks, we use the most recently updated values of the vectors of unknowns associated with the other two blocks. The coupled, linear equation system that needs to be solved in updating each of the three vectors

of unknowns is also solved iteratively, with the GMRES search technique [22]. We have implemented these solution techniques for distributed-memory parallel computing, and the results reported here were obtained by carrying out the computations on a CRAY T3E-1200.

In Section 2, we review the governing equations of fluid and structural mechanics. The finite element formulations for fluid mechanics are described in Section 3, and the finite element formulation for structural mechanics is described in Section 4. The MDM is reviewed in Section 5. The numerical examples are presented in Section 6, and the concluding remarks are provided in Section 7.

2. GOVERNING EQUATIONS

2.1 Fluid Mechanics

Let $\Omega_t \subset I\!R^{n_{sd}}$ be the spatial fluid mechanics domain with boundary Γ_t at time $t \in (0,T)$, where the subscript t indicates the time-dependence of the spatial domain and its boundary. The Navier-Stokes equations of incompressible flows can be written as

$$\rho\left(\frac{\partial \mathbf{u}}{\partial t} + \mathbf{u}\cdot\nabla\mathbf{u} - \mathbf{f}\right) - \nabla\cdot\boldsymbol{\sigma} = 0 \qquad \text{on } \Omega_t \quad \forall t \in (0,T), \tag{1}$$

$$\nabla\cdot\mathbf{u} = 0 \qquad \text{on } \Omega_t \quad \forall t \in (0,T), \tag{2}$$

where ρ, $\mathbf{u}$ and $\mathbf{f}$ are the density, velocity and the external force, respectively. The stress tensor $\boldsymbol{\sigma}$ is defined as

$$\boldsymbol{\sigma}(p,\mathbf{u}) = -p\mathbf{I} + 2\mu\boldsymbol{\varepsilon}(\mathbf{u}). \tag{3}$$

Here p, $\mathbf{I}$ and μ are the pressure, identity tensor and the viscosity, respectively. The strain rate tensor $\boldsymbol{\varepsilon}(\mathbf{u})$ is defined as

$$\boldsymbol{\varepsilon}(\mathbf{u}) = \frac{1}{2}\left((\nabla\mathbf{u}) + (\nabla\mathbf{u})^T\right). \tag{4}$$

Both Dirichlet- and Neumann-type boundary conditions are accounted for:

$$\begin{aligned} \mathbf{u} &= \mathbf{g} \text{ on } (\Gamma_t)_g, \\ \mathbf{n}\cdot\boldsymbol{\sigma} &= \mathbf{h} \text{ on } (\Gamma_t)_h. \end{aligned} \tag{5}$$

Here $(\Gamma_t)_g$ and $(\Gamma_t)_h$ are complementary subsets of the boundary Γ_t, $\mathbf{n}$ is the unit normal vector at the boundary, and $\mathbf{g}$ and $\mathbf{h}$ are given functions. A divergence-free velocity field is specified as the initial condition.

2.2 Structural Mechanics

Let $\Omega_t^s \subset I\!R^{n_{xd}}$ be the spatial structural mechanics domain with boundary Γ_t^s at time $t \in (0,T)$, where the superscript s implies structural mechanics, and $n_{xd} = 2$ for membranes and $n_{xd} = 1$ for cables. The governing equations obtained from conservation of linear momentum are written as follows:

$$\rho^s\left(\frac{d^2\mathbf{y}}{dt^2} - \mathbf{f}^s\right) - \nabla\cdot\boldsymbol{\sigma}^s = 0 \quad \text{on } \Omega_t^s \quad \forall t \in (0,T). \tag{6}$$

Here ρ^s, $\mathbf{y}$, $\mathbf{f}^s$ and $\boldsymbol{\sigma}^s$ are the material density, displacements, external body forces, and Cauchy stress tensor, respectively. In this study, we assume small strains, and therefore use linear stress-strain relations for the membrane and cable structures. However, the large displacements and rotations involved makes this class of problems nonlinear. For the membrane elements, plane stress conditions are assumed, and therefore the constitutive equations are written as follows:

$$S^{ij} = \{\overline{\lambda}_m G^{ij}G^{kl} + \mu_m(G^{il}G^{jk} + G^{ik}G^{jl})\}E_{kl}, \tag{7}$$

where,

$$\overline{\lambda}_m = \frac{2\lambda_m \mu_m}{(\lambda_m + 2\mu_m)}. \tag{8}$$

Here λ_m and μ_m are the Lamé constants, the subscript m denotes the membrane, and G^{ij} are the components of the contravariant metric tensor [23, 24]. For the cable elements, uniaxial stress condition is assumed, and therefore the constitutive equation becomes:

$$S^{11} = E_c G^{11} G^{11} E_{11}, \tag{9}$$

where E_c is the Young's modulus and the subscript c denotes the cable. Both Dirichlet- and Neumann-type boundary conditions are considered, and are expressed as:

$$\begin{aligned} \mathbf{y} &= \mathbf{g}^s \text{ on } (\Gamma_t^s)_g, \\ \mathbf{n} \cdot \boldsymbol{\sigma}^s &= \mathbf{h}^s \text{ on } (\Gamma_t^s)_h. \end{aligned} \tag{10}$$

Here $(\Gamma_t^s)_g$ and $(\Gamma_t^s)_h$ are complementary subsets of the boundary Γ_t^s, and $\mathbf{g}^s$ and $\mathbf{h}^s$ are given functions. The initial conditions are specified as

$$\mathbf{y} = \mathbf{0}, \quad \frac{d\mathbf{y}}{dt} = \mathbf{0} \text{ on } \Omega_0^s. \tag{11}$$

3. FINITE ELEMENT FORMULATIONS FOR INCOMPRESSIBLE FLOWS

3.1 Semi-Discrete Stabilized Formulation

Let us consider a fixed spatial domain Ω and its boundary Γ, where subscript t is dropped from both Ω_t and Γ_t. The domain Ω is discretized into sub-domains Ω^e, $e = 1, 2, \cdots, n_{el}$, where n_{el} is the number of elements. For this discretization, the finite element trial function spaces $\mathcal{S}_u^h$ for velocity and $\mathcal{S}_p^h$ for pressure, and the corresponding test function spaces $\mathcal{V}_u^h$ and $\mathcal{V}_p^h$ are defined as follows:

$$\mathcal{S}_u^h = \{\mathbf{u}^h | \mathbf{u}^h \in [H^{1h}(\Omega)]^{n_{sd}}, \mathbf{u}^h \doteq \mathbf{g}^h \; on \; \Gamma_g\}, \tag{12}$$

$$\mathcal{V}_u^h = \{\mathbf{w}^h | \mathbf{w}^h \in [H^{1h}(\Omega)]^{n_{sd}}, \mathbf{w}^h \doteq \mathbf{0} \; on \; \Gamma_g\}, \tag{13}$$

$$\mathcal{S}_p^h = \mathcal{V}_p^h = \{q^h | q^h \in H^{1h}(\Omega)\}. \tag{14}$$

Here $H^{1h}(\Omega)$ is the finite-dimensional function space over Ω. The stabilized finite element formulation is written as follows: find $\mathbf{u}^h \in \mathcal{S}_{\mathbf{u}}^h$ and $p^h \in \mathcal{S}_p^h$ such that $\forall \mathbf{w}^h \in \mathcal{V}_{\mathbf{u}}^h$ and $q^h \in \mathcal{V}_p^h$:

$$\begin{aligned} & \int_\Omega \mathbf{w}^h \cdot \rho \left(\frac{\partial \mathbf{u}^h}{\partial t} + \mathbf{u}^h \cdot \boldsymbol{\nabla} \mathbf{u}^h - \mathbf{f}^h \right) d\Omega \\ + & \int_\Omega \boldsymbol{\varepsilon}(\mathbf{w}^h) : \boldsymbol{\sigma}(p^h, \mathbf{u}^h) d\Omega \\ - & \int_{\Gamma_h} \mathbf{w}^h \cdot \mathbf{h}^h d\Gamma \\ + & \int_\Omega q^h \boldsymbol{\nabla} \cdot \mathbf{u}^h d\Omega \\ + & \sum_{e=1}^{n_{el}} \int_{\Omega^e} \frac{1}{\rho} [\tau_{\text{SUPG}} \rho \mathbf{u}^h \cdot \nabla \mathbf{w}^h + \tau_{\text{PSPG}} \nabla q^h] \cdot \end{aligned}$$

$$
\begin{aligned}
& \left[\rho\left(\frac{\partial \mathbf{u}^h}{\partial t}+\mathbf{u}^h\cdot\boldsymbol{\nabla}\mathbf{u}^h\right)-\boldsymbol{\nabla}\cdot\boldsymbol{\sigma}(p^h,\mathbf{u}^h)-\rho\mathbf{f}^h\right]d\Omega \\
+ & \sum_{e=1}^{n_{el}}\int_{\Omega^e}\tau_{\mathrm{LSIC}}\boldsymbol{\nabla}\cdot\mathbf{w}^h\rho\boldsymbol{\nabla}\cdot\mathbf{u}^h d\Omega \\
= & \ 0. \qquad (15)
\end{aligned}
$$

In this formulation, τ_{SUPG}, τ_{PSPG} and τ_{LSIC} are the stabilization parameters (see [7]). For an earlier, detailed reference on this stabilized formulation see [8].

3.2 Deforming-Spatial-Domain/Stabilized Space-Time (DSD/SST) Formulation

In discretization of the space-time domain, the time interval $(0,T)$ is partitioned into subintervals $I_n = (t_n, t_{n+1})$, where t_n and t_{n+1} belong to an ordered series of time levels $0 = t_0 < t_1 \cdots < t_N = T$. Let $\Omega_n = \Omega_{t_n}$ and $\Gamma_n = \Gamma_{t_n}$ to simplify the notation. The space-time slab Q_n is defined as the domain enclosed by the surfaces Ω_n, Ω_{n+1}, and P_n, where P_n is the lateral surface of Q_n described by the boundary Γ_n as t traverses I_n. The Dirichlet- and Neumann-type boundary conditions are specified over $(P_n)_g$ and $(P_n)_h$. For this discretization, the finite element trial function spaces $(\mathcal{S}^h_{\mathbf{u}})_n$ for velocity and $(\mathcal{S}^h_p)_n$ for pressure, and the corresponding test function spaces $(\mathcal{V}^h_{\mathbf{u}})_n$ and $(\mathcal{V}^h_p)_n$ are defined as follows:

$$(\mathcal{S}^h_{\mathbf{u}})_n = \{\mathbf{u}^h | \mathbf{u}^h \in [H^{1h}(Q_n)]^{n_{sd}}, \mathbf{u}^h \doteq \mathbf{g}^h \ on \ (P_n)_g\}, \qquad (16)$$

$$(\mathcal{V}^h_{\mathbf{u}})_n = \{\mathbf{w}^h | \mathbf{w}^h \in [H^{1h}(Q_n)]^{n_{sd}}, \mathbf{w}^h \doteq \mathbf{0} \ on \ (P_n)_g\}, \qquad (17)$$

$$(\mathcal{S}^h_p)_n = (\mathcal{V}^h_p)_n = \{q^h | q^h \in H^{1h}(Q_n)\}. \qquad (18)$$

Here $H^{1h}(Q_n)$ is the finite-dimensional function space over the space-time slab Q_n. Over the element domain, this space is formed by using first-order polynomials in both space and time. The interpolation functions are continuous in space but discontinuous in time.

The DSD/SST formulation is written as follows: given $(\mathbf{u}^h)^-_n$, find $\mathbf{u}^h \in (\mathcal{S}^h_{\mathbf{u}})_n$ and $p^h \in (\mathcal{S}^h_p)_n$ such that $\forall \mathbf{w}^h \in (\mathcal{V}^h_{\mathbf{u}})_n$ and $q^h \in (\mathcal{V}^h_p)_n$:

$$
\begin{aligned}
& \int_{Q_n}\mathbf{w}^h\cdot\rho\left(\frac{\partial \mathbf{u}^h}{\partial t}+\mathbf{u}^h\cdot\boldsymbol{\nabla}\mathbf{u}^h-\mathbf{f}^h\right)dQ \\
+ & \int_{Q_n}\boldsymbol{\varepsilon}(\mathbf{w}^h):\boldsymbol{\sigma}(p^h,\mathbf{u}^h)dQ \\
- & \int_{(P_n)_h}\mathbf{w}^h\cdot\mathbf{h}^h dP \\
+ & \int_{Q_n}q^h\boldsymbol{\nabla}\cdot\mathbf{u}^h dQ \\
+ & \int_{\Omega_n}(\mathbf{w}^h)^+_n\cdot\rho\left((\mathbf{u}^h)^+_n-(\mathbf{u}^h)^-_n\right)d\Omega \\
+ & \sum_{e=1}^{(n_{el})_n}\int_{Q^e_n}\frac{\tau_{\mathrm{LSME}}}{\rho}\left[\rho\left(\frac{\partial \mathbf{w}^h}{\partial t}+\mathbf{u}^h\cdot\boldsymbol{\nabla}\mathbf{w}^h\right)-\boldsymbol{\nabla}\cdot\boldsymbol{\sigma}(q^h,\mathbf{w}^h)\right]\cdot \\
& \left[\rho\left(\frac{\partial \mathbf{u}^h}{\partial t}+\mathbf{u}^h\cdot\boldsymbol{\nabla}\mathbf{u}^h\right)-\boldsymbol{\nabla}\cdot\boldsymbol{\sigma}(p^h,\mathbf{u}^h)-\rho\mathbf{f}^h\right]dQ
\end{aligned}
$$

$$
\begin{aligned}
&+ \quad \sum_{e=1}^{n_{el}} \int_{Q_n^e} \tau_{\text{LSIC}} \boldsymbol{\nabla} \cdot \mathbf{w}^h \rho \boldsymbol{\nabla} \cdot \mathbf{u}^h dQ \\
&= \quad 0. \qquad (19)
\end{aligned}
$$

This formulation is sequentially applied to all space-time slabs $Q_0, Q_1, Q_2, \ldots, Q_{N-1}$. The computation starts with

$$(\mathbf{u}^h)_0^- = \mathbf{u}_0, \quad \boldsymbol{\nabla} \cdot \mathbf{u}_0 = 0 \quad \text{on } \Omega_0. \qquad (20)$$

Here τ_{LSME} and τ_{LSIC} are the stabilization parameters (see [7, 25]). For an earlier, detailed reference on this stabilized formulation see [8].

4. FINITE ELEMENT FORMULATION FOR STRUCTURAL MECHANICS

Consider Ω^s as the spatial structural mechanics domain where the subscript t has been dropped to simplify the notation. The domain Ω^s is discretized into sub-domains $(\Omega^s)^e$, $e = 1, 2, \cdots, n_{el}^s$, where n_{el}^s is the number of structural mechanics elements. For this discretization, the finite element trial function space $\mathcal{S}^h$ for displacement, and the corresponding test function space $\mathcal{V}^h$ are defined as follows:

$$\mathcal{S}^h = \{\mathbf{y}^h | \mathbf{y}^h \in [H^{1h}(\Omega^s)]^{n_{sd}}, \mathbf{y}^h \doteq (\mathbf{g}^s)^h \; on \; \Gamma_g^s\}, \qquad (21)$$

$$\mathcal{V}^h = \{\delta\mathbf{y}^h | \delta\mathbf{y}^h \in [H^{1h}(\Omega^s)]^{n_{sd}}, \delta\mathbf{y}^h \doteq \mathbf{0} \; on \; \Gamma_g^s\}. \qquad (22)$$

Here $H^{1h}(\Omega^s)$ is the finite-dimensional function space over Ω^s. Applying the principle of virtual work, the finite element formulation is written as follows: find $\mathbf{y}^h \in \mathcal{S}^h$ such that $\forall \delta\mathbf{y}^h \in \mathcal{V}^h$:

$$\int_{\Omega^s} \rho^s \frac{d^2\mathbf{y}^h}{dt^2} \cdot \delta\mathbf{y}^h d\Omega^s + \int_{\Omega^s} \mathbf{S}^h : \delta\mathbf{E}^h d\Omega^s = \int_{\Gamma_h^s} (\mathbf{h}^s)^h \cdot \delta\mathbf{y}^h d\Gamma^s + \int_{\Omega^s} \rho^s \mathbf{f}^h \cdot \delta\mathbf{y}^h d\Omega^s. \qquad (23)$$

5. MULTI-DOMAIN METHOD (MDM)

In the MDM, in addition to dividing the problem into computationally more manageable pieces, we can use different numerical methods for different subdomains. With this approach, the method used for a subdomain is the most effective one for the flow conditions of that subdomain. Furthermore, in the MDM, in addition to using parallel computation for each subdomain where clusters of elements in that subdomain are assigned to different processors, we find a second level of parallelism. This second parallelism is based on recognizing that the computation for each subdomain needs to lag only one time step behind the subdomain preceding it. In fact different subdomains can be assigned to different computers, or can even be assigned to computers at different geographical locations. This is because only 2D data needs to be transferred between the subdomains, and this does not result in as much of a communication burden as transferring 3D data.

Subdomain-1 contains a complex but fixed object, and consequently does not involve any changes in the spatial domain occupied by the fluid. Therefore, for Subdomain-1 we use a general-purpose implementation of the semi-discrete formulation. In the general-purpose implementation, we assume that the elements of the tetrahedral finite element mesh can be of any shape. Subdomain-2 does not involve any objects, and therefore is handled with a special-purpose implementation of the semi-discrete formulation, where the mesh is assumed to be made of box-shaped hexahedral elements. The special-purpose implementation exploits the simplicity of the mesh to increase the computational speed (see [16]). Furthermore, to capture the details of the wake behavior more accurately, the method used in Subdomain-2 is supplemented with the Enhanced-Discretization Interface-Capturing Technique (EDICT).

The EDICT was first introduced in [26] for the purpose of increasing the accuracy in representing the interface in computation of a two-fluid flow problem with an interface-capturing method. To enhance the discretization near the interfaces, the finite element functions are defined as functions with multiple components, with each component coming from a different level of finite element mesh. Mesh-1 is the base mesh, and a Mesh-2 is generated by constructing a second-level mesh over a subset of the elements in Mesh-1. This subset of elements in Mesh-1 changes periodically during the computation, and as the interface moves, it is enveloped in regions covered by this subset of elements. For further details on the EDICT, see [27]. The EDICT was later extended in [28] to computation of compressible flows with shocks. This extension is based on re-defining the "interface" to mean the shock front, and at and near the shock fronts enhanced discretization is used to increase the accuracy in representing those shocks. In the extension of the EDICT to computation of vortex flows, the definition of the interface is extended to mean regions where the vorticity magnitude is larger than a specified value. This version of the EDICT gives us the capability to compute the long-wake flows more accurately, without making the computations too costly.

Subdomain-3 contains a complex object that can move and change its shape. Therefore, the computation over Subdomain-3 is based on a general-purpose implementation of the DSD/SST formulation and a tetrahedral mesh.

For computations over Subdomain-1 and Subdomain-3, we use a Smagorinsky turbulence model [29] with its constant $C = 0.15$, and wall damping based on what has been proposed by Van Driest [30].

6. NUMERICAL EXAMPLES

6.1 Aerodynamics of a Paratrooper Separating from an Aircraft

The aircraft is traveling at 130 knots, with an angle of attack of 10 degrees. We assume symmetry with respect to the vertical plane passing through the middle of the aircraft. The original aircraft model was introduced in [6]. An improved geometric model, generated by including the wing flaps and winglets, was introduced in [7]. In the simulation we describe here, which we reported in [4], we use the improved aircraft model and a more realistic model of the paratrooper. In defining the parameters of the problem with non-dimensional numbers, the length of the aircraft (nose to tail wingtip) is taken as 8.81 units, and the flight speed as 1.0 unit. The boundary conditions consist of uniform upstream velocity, no-slip on the aircraft and paratrooper surfaces, zero normal velocity and zero shear stress at the crossflow and side boundaries, and traction-free condition at the outflow boundary. For the engines, the intake and exhaust flow velocity profiles are assumed to be uniform, and prescribed as 1.0 and 3.0, respectively. The tetrahedral mesh has 129,090 nodes and 728,902 elements. We realize that these mesh refinement levels are below the levels required to secure quantitatively dependable solutions for the complex flow problems we are addressing here. However, we see these computations as demonstrations of the tools we have been developing for this class of problems, and also as a way of having a general, qualitative understanding of the solution in each problem. The parallel computation was carried on a CRAY T3E-1200. Figure 2 shows the aircraft and the paratrooper in the early stages of the separation. Figure 3 shows the close-up view of the flow field around the paratrooper.

6.2 Fluid-Structure Interactions of a Parachute Crossing the Far Wake of an Aircraft

This simulation was reported in [2]. Simulation of the aerodynamics of a rigid parachute crossing the far wake of an aircraft was presented in [1], which included the MDM-based computations for the flow around the aircraft in Subdomain-1 and the long-wake flow in Subdomain-2. The flow around the parachute is computed in Subdomain-3.

The aircraft is assumed to be traveling at $200 ft/s$, with an angle of attack of 10 degrees. In defining the parameters of the problem with non-dimensional numbers, the length of the aircraft is taken as 10 units, and

the flight speed as 1.0 unit. The long-wake flow computed in [1] is used here to define the flow conditions the parachute is subjected to as it traverses the space also covered by the wake domain.

Subdomain-1 and Subdomain-2 computations were carried out in a coordinate frame attached to the aircraft, and we take this into account when we extract the boundary conditions for Subdomain-3. We assume that the aircraft that deployed the parachute is flying at the same speed as the aircraft that generated the wake: $200ft/s$. We also assume that at the end of a short, initial period following the deployment of the parachute, its horizontal velocity becomes zero in a coordinate frame attached to the ground, and it attains a descent velocity of $20ft/s$. Based on these conditions, we can approximate the trajectory of the parachute as a parabolic curve (corresponding to the short, initial period), and an oblique line with a tangent of 0.1 (corresponding to the period when the parachute has zero horizontal velocity and a descent velocity of $20ft/s$) (see Figure 4). Here we focus on the trajectory phase represented by the oblique line. Furthermore, we select approximately the midpoint between the wingtip and the outer engine as the lateral position relative to the aircraft that the parachute crosses the wake.

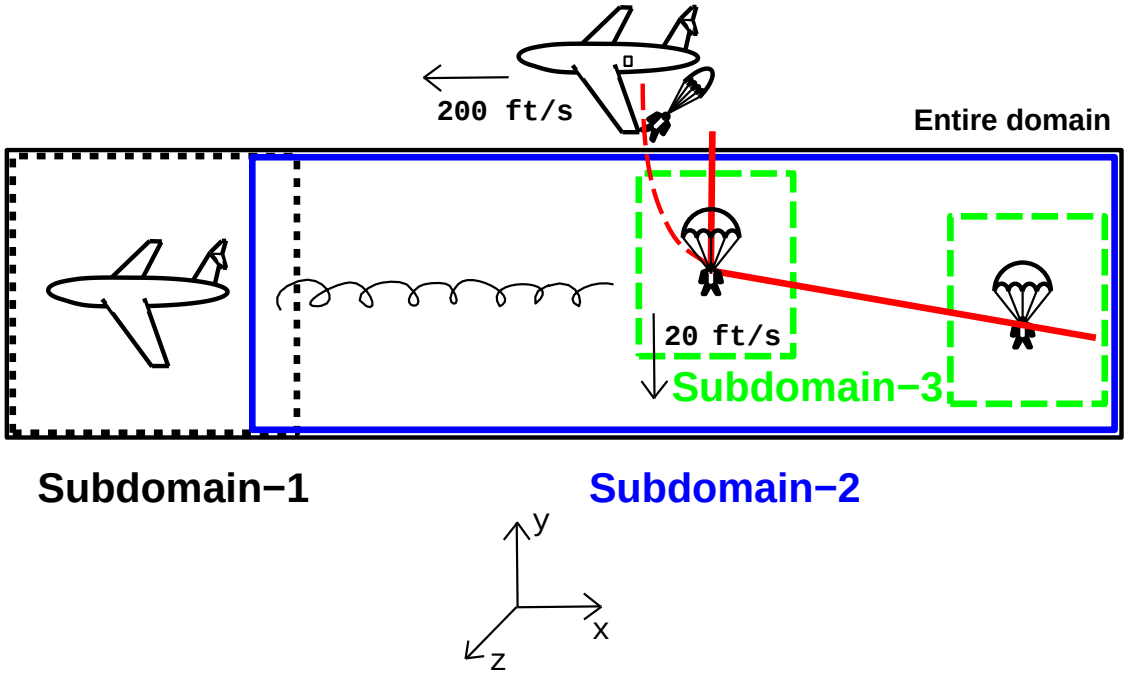

Figure 4. Fluid-structure interactions of a parachute crossing the far wake of an aircraft. Parachute trajectory in a coordinate frame attached to the aircraft. The broken line starting from the aircraft shows the assumed trajectory in the short, initial period prior to the parachute attaining zero horizontal velocity and $20ft/s$ decent velocity. The oblique line following that shows the trajectory after this initial period. The short, vertical line shows the trajectory used in the computations corresponding to the short, initial period.

The parachute is modeled after a US Army C–9 personnel parachute, with 28 suspension lines. These lines extend through the canopy as reinforcements. We include a barrel-shaped payload in our model. This payload is positioned relative to the parachute in such a way that the suspension lines join at the top of the payload.

The structural model for the parachute starts with a canopy that is flat and of circular shape. The finite element mesh for the parachute structure is made of 4,509 nodes, 8,288 triangular membrane elements, and 1,120 two-noded cable elements (see the left picture in Figure 5). The parallel computations were carried

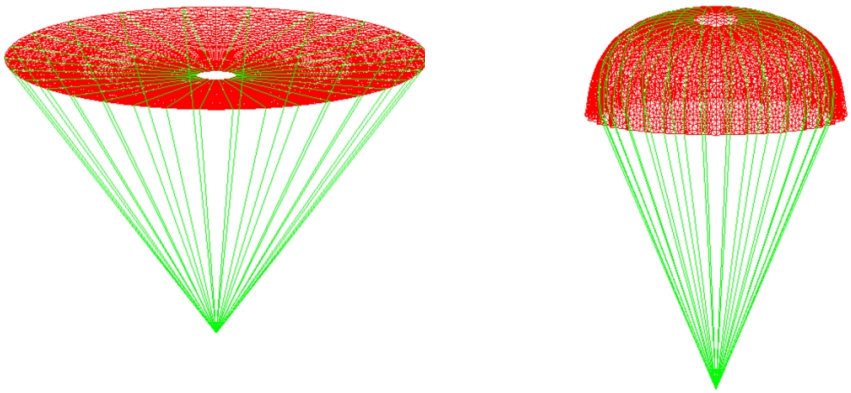

Figure 5. Fluid-structure interactions of a parachute crossing the far wake of an aircraft. Mesh for the parachute structure. Initial (left) and inflated (right) geometries.

on a CRAY T3E-1200. First a stand-alone structural mechanics computation is carried out to inflate the canopy with a uniform pressure differential prescribed on the canopy surface. After this inflation, the canopy diameter and height become approximately 1.2 and 0.6, respectively (see the right picture in Figure 5). This inflated shape is used in defining the initial conditions for the structure in computation of the fluid-structure interactions. The Reynolds number based on the parachute diameter and the typical descent velocity of $20ft/s$ is 2×10^6.

Using the triangular mesh for the canopy as an interior surface mesh, a volume mesh in generated for the fluid domain. This mesh is made of 212,177 nodes, 1,286,063 tetrahedral elements in the interior, and 10,089 prismatic elements in the one-element-thick layer surrounding the domain (see Figure 6).

The boundary conditions for the fluid dynamics part of the problem consist of inflow conditions at the bottom and side boundaries, outflow conditions at the top boundary, and no-slip on the parachute and payload surfaces. The velocity conditions at the inflow and the stress conditions at the outflow are extracted from the wake flow data computed in [1]. The extracted velocity boundary conditions are modified to take into account the parachute trajectory. In describing the results here, $t = 0$ marks the beginning of the trajectory phase represented by the oblique line in Figure 4. In this computation the time step size is 0.005.

We compare the computed results with those obtained for a parachute descending through a wake-free air (and therefore subjected to uniform flow conditions). Figure 7 shows the pressure distribution on the upper and lower surfaces of the parachute canopy for the parachute in uniform flow and, at two different instants, for the parachute crossing the aircraft's wake. We note that the pressure on the lower surface is always higher than it is on the upper surface. Figure 8 shows the aerodynamical forces acting on the parachute for the one in uniform flow and the one in the wake. Figure 9 shows the distribution of the maximum principal stress for the canopy. The stresses for the parachute crossing the wake are displayed at the same time steps as those in Figure 7. We note the non-symmetric deformation of the parachute canopy at those time steps.

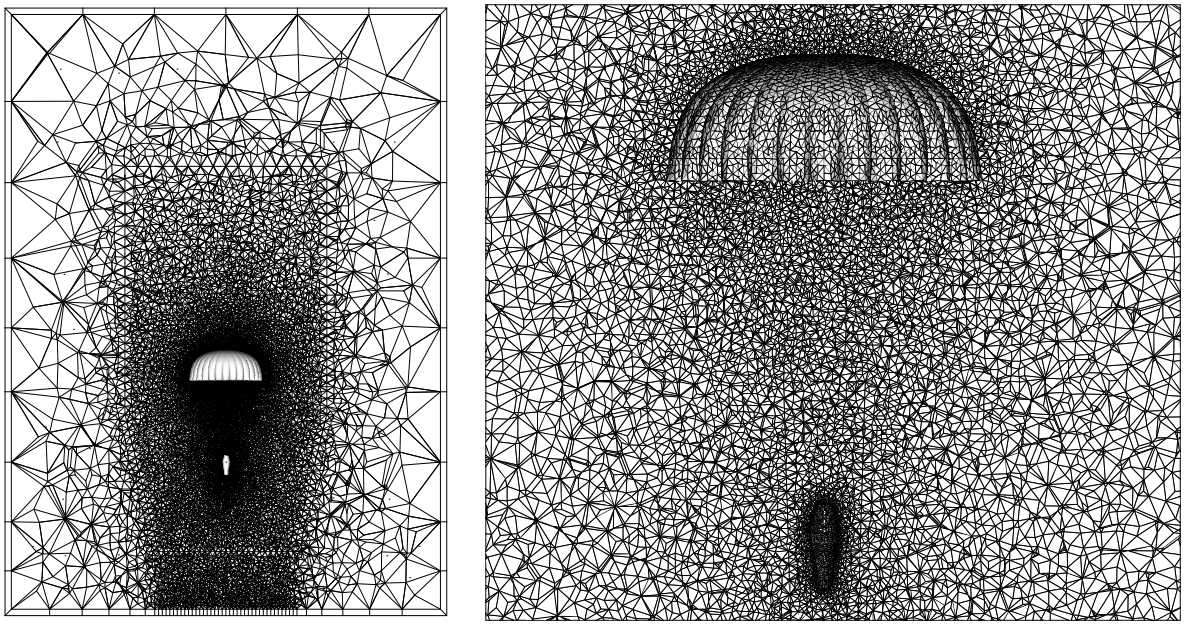

Figure 6. Fluid-structure interactions of a parachute crossing the far wake of an aircraft. Initial mesh for the parachute domain.

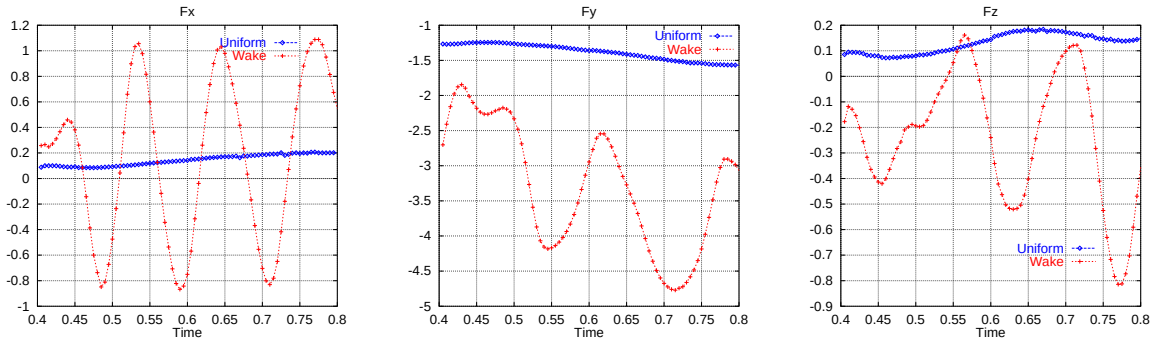

Figure 8. Fluid-structure interactions of a parachute crossing the far wake of an aircraft. Time history of the aerodynamical forces acting on the parachute for the one in uniform flow and the one in the wake. Graphs show the forces in the aircraft's flight direction (left), the vertical drag (middle), and the force in lateral direction (right).

6.3 Aerodynamic Interactions Between Two Separate Parachutes

In this set of simulations, which were reported in [5], we study the aerodynamic interactions between two separate parachutes when the two paratroopers come close to each other. The parachute canopy model

represents the US Army C–9 parachute. A model representing the paratrooper includes the typical items carried by the paratrooper. We carry out computations with the horizontal distance between the paratroopers ranging from zero parachute radii to five. The vertical distance is kept constant, where the distance between the feet of the upper paratrooper and the apex of the lower canopy is approximately one meter. The left picture in Figure 10 shows a cross-section of the fluid mechanics mesh for the case where the distance between the paratroopers is two parachute radii. The two pictures on the right show the surface meshes for the canopy and paratrooper. The parallel computations were carried out on a CRAY T3E-1200. Figure 11 shows the

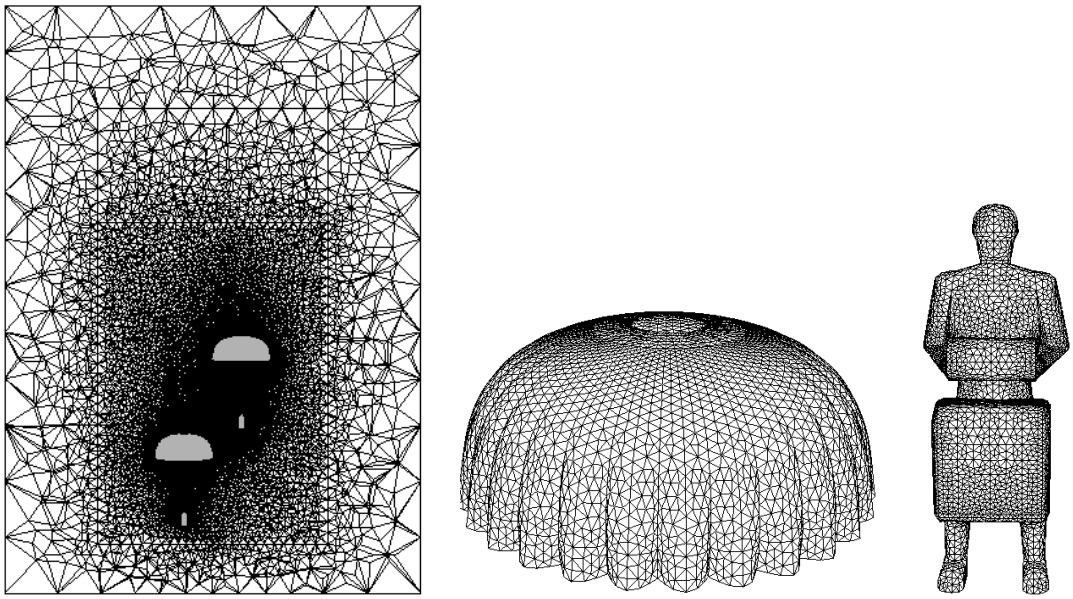

Figure 10. Aerodynamic interactions between two separate parachutes. Cross-section of the fluid mechanics mesh (left), canopy surface mesh (middle), and paratrooper surface mesh (right).

velocity and vorticity fields for parachute separation distances of 0.5, 2.0, and 5.0 radii. The simulations show that the aerodynamic interactions between the parachutes are stronger for separation distances of 1.0 radius or less. For these cases, the upper parachute experiences a loss of drag substantial enough to risk parachute collapse (see [5]). The strength of the aerodynamic interactions decreases as the separation distance increases, and becomes insignificant when the parachutes are 5.0 radii apart.

6.4 Aerodynamic Interactions Between Canopies of a Cluster of Parachutes

In this set of simulations, we study the aerodynamic interactions between the canopies of a cluster of parachutes used for a single payload. These simulations were reported in [5]. The canopy models represent the US Army C–9 parachute. The number of canopies ranges from three to six. For each of the four-canopy and five-canopy clusters, we use two different arrangement, bringing the total number of cases investigated to six. The parallel computations were carried out on a CRAY T3E-1200. The middle column of pictures in Figure 12 show the cluster configurations computed. The left and right column of pictures show, in two mutually perpendicular vertical cutting planes, the vorticity magnitude obtained from these preliminary computations. We consider these computations as the first step in investigation of this class of problems, where much needs to be done in understanding the aerodynamic behavior and in making the simulations

more realistic.

6.5 Aerodynamics of the Crew Return Vehicle and Parafoil at Different Opening Stages

These simulations were reported in [3]. The CRV model has a length of 24.2 ft and is descending at 50 ft/s. The parafoil goes through six different opening stages, and we focus on the four that are symmetric in parafoil geometry. Computations are carried out by taking each of these four stages as a separate case. Figure 13 shows the first three symmetric opening stages of the parafoil. In Stage 1, shown in the top picture, the parafoil has 11 fully disreefed cells, and the span length is 38.5 ft. Stage 2, shown in the middle picture, has 23 disreefed cells and a span length of 80.5 ft. The last picture in this figure shows Stage 3, which has 31 disreefed cells and a span length of 108.5 ft. In the the final stage, Stage 4, the parafoil has the same number of disreefed cells and span length as it did in Stage 3, but an increased radius of curvature. Figure 14 shows how the final stage is reached from Stage 3 by increasing the radius of curvature. The number of elements in the tetrahedral meshes used for the different stages of the parafoil ranges from 2.2 million to 3.5 million. The parallel computations were carried on a CRAY T3E-1200. Figure 15 shows, for the final stage of the parafoil, the air pressure distribution on the surface of the CRV and parafoil.

7. CONCLUDING REMARKS

We provided a review of some of the computational mechanics methods developed recently by the T⋆AFSM for simulation of airdrop systems. The methods include special numerical stabilization methods; Deforming-Spatial-Domain/Stabilized Space-Time formulation; Enhanced-Discretization Interface-Capturing Technique; advanced mesh update methods; Multi-Domain Method; iterative solution methods for large equation systems; and parallel and multi-platform computing strategies. The class of applications we were targeting include aerodynamics of a paratrooper separating from an aircraft; fluid-structure interactions of a parachute crossing the far wake of an aircraft; aerodynamic interactions between two separate parachutes; aerodynamic interactions between canopies of a cluster of parachutes; and aerodynamics of the Crew Return Vehicle and parafoil at different opening stages. By testing the methods developed on the applications listed above, we were able to show how advanced methods of computational mechanics are being employed to address some of the challenges encountered in simulation of airdrop systems.

ACKNOWLEDGMENT

This work was supported by NASA Johnson Space Center (grant no. NAG9-1059) and by the US Army Natick Soldier Center (contract no. DAAD16-00-C-9222). The content does not necessarily reflect the position or the policy of the government, and no official endorsement should be inferred.

References

[1] T.E. Tezduyar and Y. Osawa, "The Multi-Domain Method for computation of the aerodynamics of a parachute crossing the far wake of and aircraft", ~~to appear in~~ *Computer Methods in Applied Mechanics and Engineering*, ~~2001.~~ **191** (2001) 705-716.

[2] T.E. Tezduyar and Y. Osawa, "Fluid-structure interactions of a parachute crossing the far wake of an aircraft", ~~to appear in~~ *Computer Methods in Applied Mechanics and Engineering*, ~~2001.~~ **191** (2001) 717-726.

[3] L. Haubelt, W. Yee, and T. Tezduyar, "Aerodynamics of the crew return vehicle and parafoil at different opening stages", ~~to appear in~~ *Proceedings of the First MIT Conference on Computational Fluid and Solid Mechanics*, Boston, Massachusetts, 2001.

[4] V. Udoewa, R. Keedy, T. Nonoshita, T. Tezduyar, K. Stein, and A. Johnson, "Aerodynamic simulation of an object separating from an aircraft during initial deployment", ~~to appear in~~ *Proceedings of the First MIT Conference on Computational Fluid and Solid Mechanics*, Boston, Massachusetts, 2001.

[5] K. Stein, R. Benney, T. Tezduyar, V. Kumar, E. Thornburg, C. Kyle, and T. Nonoshita, "Aerodynamic interaction between multiple parachute canopies", ~~to appear in~~ *Proceedings of the First MIT Conference on Computational Fluid and Solid Mechanics*, Boston, Massachusetts, 2001.

[6] T.E. Tezduyar, S. Aliabadi, M. Behr, A. Johnson, V. Kalro, and M. Litke, "Flow simulation and high performance computing", *Computational Mechanics*, **18** (1996) 397–412.

[7] T.E. Tezduyar and Y. Osawa, "Methods for parallel computation of complex flow problems", *Parallel Computing*, **25** (1999) 2039–2066.

[8] T.E. Tezduyar, "Stabilized finite element formulations for incompressible flow computations", *Advances in Applied Mechanics*, **28** (1991) 1–44. ⟵ (1992)

[9] T.E. Tezduyar, M. Behr, and J. Liou, "A new strategy for finite element computations involving moving boundaries and interfaces – the deforming-spatial-domain/space-time procedure: I. The concept and the preliminary tests", *Computer Methods in Applied Mechanics and Engineering*, **94** (1992) 339–351.

[10] T.E. Tezduyar, M. Behr, S. Mittal, and J. Liou, "A new strategy for finite element computations involving moving boundaries and interfaces – the deforming-spatial-domain/space-time procedure: II. Computation of free-surface flows, two-liquid flows, and flows with drifting cylinders", *Computer Methods in Applied Mechanics and Engineering*, **94** (1992) 353–371.

[11] T.J.R. Hughes and G.M. Hulbert, "Space-time finite element methods for elastodynamics: formulations and error estimates", *Computer Methods in Applied Mechanics and Engineering*, **66** (1988) 339–363.

[12] T.J.R. Hughes, L.P. Franca, and G.M. Hulbert, "A new finite element formulation for computational fluid dynamics: VIII. the Galerkin/least-squares method for advective-diffusive equations", *Computer Methods in Applied Mechanics and Engineering*, **73** (1989) 173–189.

[13] T.J.R. Hughes and A.N. Brooks, "A multi-dimensional upwind scheme with no crosswind diffusion", in T.J.R. Hughes, editor, *Finite Element Methods for Convection Dominated Flows*, AMD-Vol.34, 19–35, ASME, New York, 1979.

[14] A.N. Brooks and T.J.R. Hughes, "Streamline upwind/Petrov-Galerkin formulations for convection dominated flows with particular emphasis on the incompressible Navier-Stokes equations", *Computer Methods in Applied Mechanics and Engineering*, **32** (1982) 199–259.

[15] T.E. Tezduyar, M. Behr, S. Mittal, and A.A. Johnson, "Computation of unsteady incompressible flows with the finite element methods – space-time formulations, iterative strategies and massively parallel implementations", in P. Smolinski, W.K. Liu, G. Hulbert, and K. Tamma, editors, *New Methods in Transient Analysis*, AMD-Vol.143, ASME, New York, (1992) 7–24.

[16] Y. Osawa, V. Kalro, and T.E. Tezduyar, "Multi-domain parallel computation of wake flows", *Computer Methods in Applied Mechanics and Engineering*, **174** (1999) 371–391.

[17] Y. Osawa and T.E. Tezduyar, "A multi-domain method for 3D computation of wake flow behind a circular cylinder", *Computational Fluid Dynamics Journal*, **8** (1999) 296–308.

[18] Y. Osawa and T.E. Tezduyar, "3D simulation and visualization of unsteady wake flow behind a cylinder", *Journal of Visualization*, **2** (1999) 127–134.

[19] K. Stein, R. Benny, V. Kalro, , T.E. Tezduyar, J. Leonard, and M. Accorsi, "Parachute fluid-structure interactions: 3-D Computation", *Computer Methods in Applied Mechanics and Engineering*, **190** (2000) 373–386.

[20] V. Kalro and T.E. Tezduyar, "A parallel 3D computational method for fluid-structure interactions in parachute systems", *Computer Methods in Applied Mechanics and Engineering*, **190** (2000) 321–332.

[21] T.E. Tezduyar, V. Kalro, and W. Garrard, "Parallel computational methods for 3D simulation of a parafoil with prescribed shape changes", *Parallel Computing*, **23** (1997) 1349–1363.

[22] Y. Saad and M. Schultz, "GMRES: A generalized minimal residual algorithm for solving nonsymmetric linear systems", *SIAM Journal of Scientific and Statistical Computing*, **7** (1986) 856–869.

[23] K.J. Bathe, *Finite Element Procedures*. Prentice-Hall, Inc., 1996.

[24] A. Lo, *Nonlinear Dynamic Analysis of Cable and Membrane Structure*, Ph.D. thesis, Department of Civil Engineering, Oregon State University, 1982.

[25] M. Behr and T.E. Tezduyar, "Finite element solution strategies for large-scale flow simulations", *Computer Methods in Applied Mechanics and Engineering*, **112** (1994) 3–24.

[26] T.E. Tezduyar, S. Aliabadi, and M. Behr, "Enhanced-Discretization Interface-Capturing Technique", in Y. Matsumoto and A. Prosperetti, editors, *Proceedings of the ISAC '97 High Performance Computing on Multiphase Flows*, 1–6, Japan Society of Mechanical Engineers, 1997.

[27] T.E. Tezduyar, S. Aliabadi, and M. Behr, "Enhanced-Discretization Interface-Capturing Technique (EDICT) for computation of unsteady flows with interfaces", *Computer Methods in Applied Mechanics and Engineering*, **155** (1998) 235–248.

[28] S. Mittal, S. Aliabadi, and T.E. Tezduyar, "Parallel computation of unsteady compressible flows with the EDICT", *Computational Mechanics*, **23** (1999) 151–157.

[29] J. Smagorinsky, "General circulation experiments with the primitive equations", *Monthly Weather Review*, **91** (1963) 99–165.

[30] E.R. Van Driest, "On turbulent flow near a wall", *Journal of Aerospace Science*, **1** (1956) 1007–1011.

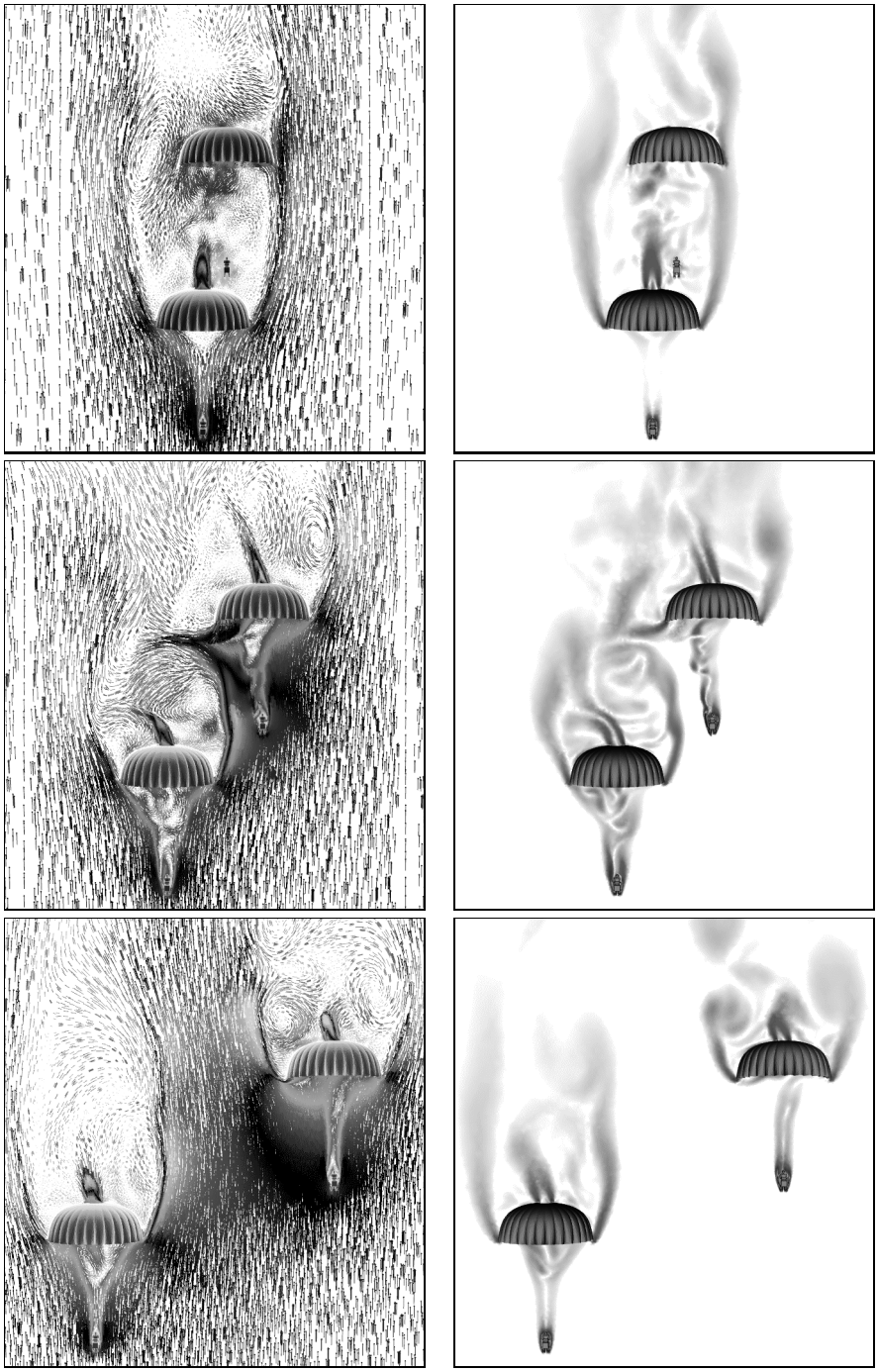

Figure 11. Aerodynamic interactions between two separate parachutes. Velocity (left) and vorticity (right) fields for separation distances of 0.5 (top), 2.0 (middle), and 5.0 (bottom) radii.

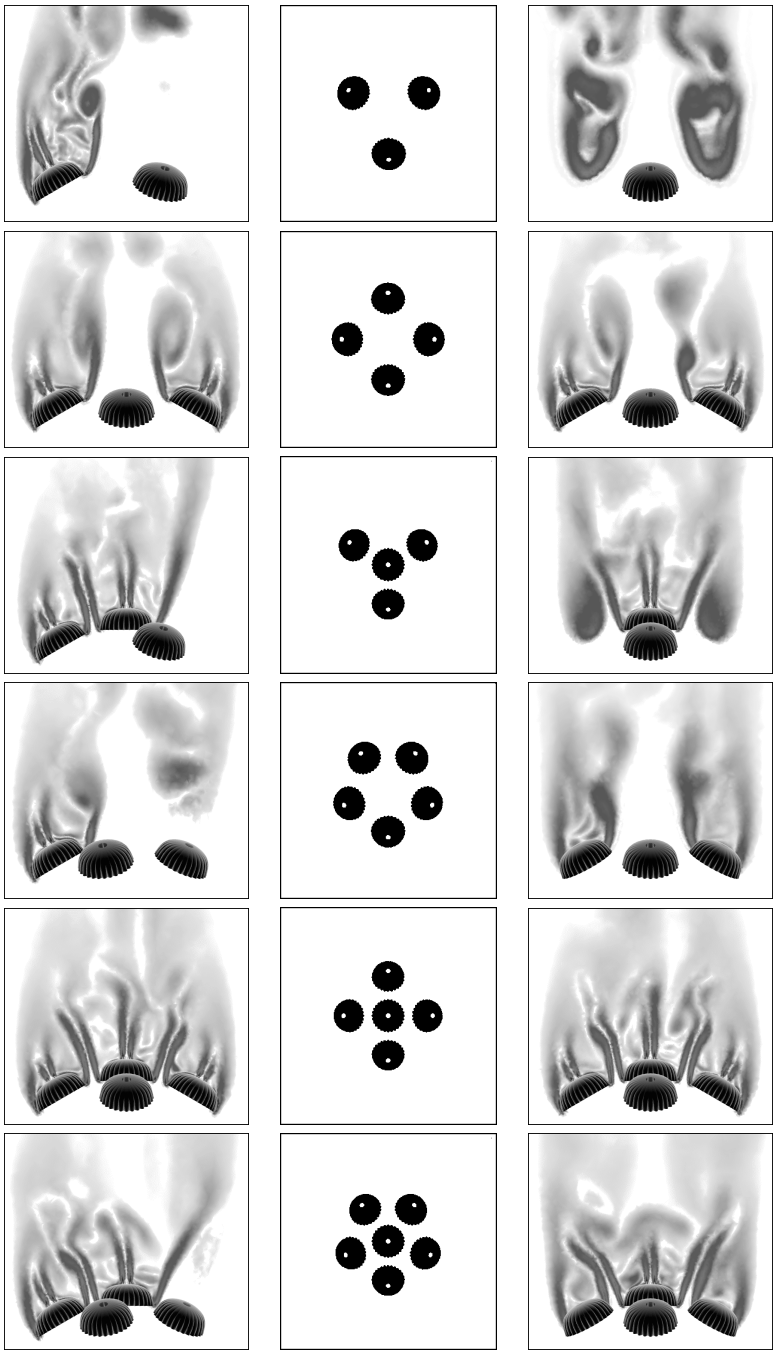

Figure 12. Aerodynamic interactions between canopies of a cluster of parachutes. Cluster configurations (middle) and vorticity magnitude in two mutually perpendicular vertical cutting planes (left and right).

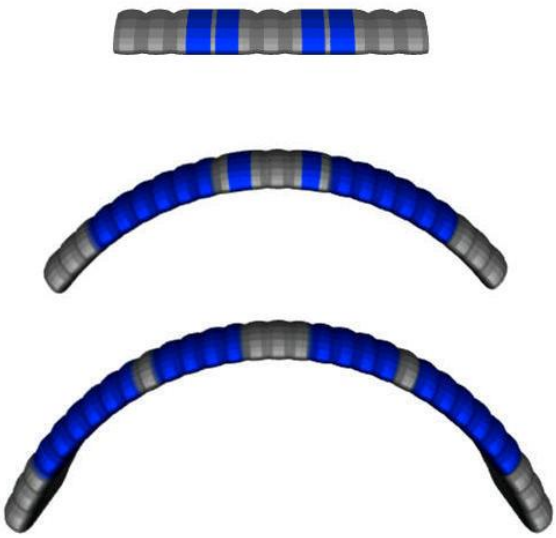

Figure 13. Aerodynamics of the Crew Return Vehicle and parafoil at different opening stages. First three symmetric stages of the parafoil. Top: Stage 1 (11 disreefed cells, span length = 38.5 ft); Middle: Stage 2 (23 disreefed cells, span length = 80.5 ft); Bottom: Stage 3 (31 disreefed cells, span length = 108.5 ft).

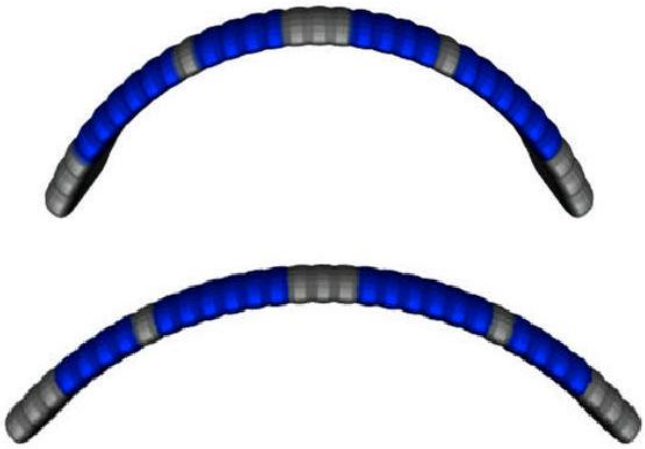

Figure 14. Aerodynamics of the Crew Return Vehicle and parafoil at different opening stages. Final stage of the parafoil is reached by increasing the radius of curvature of Stage 3. Top: Stage 3 prior to the increase; Bottom: after the increase.

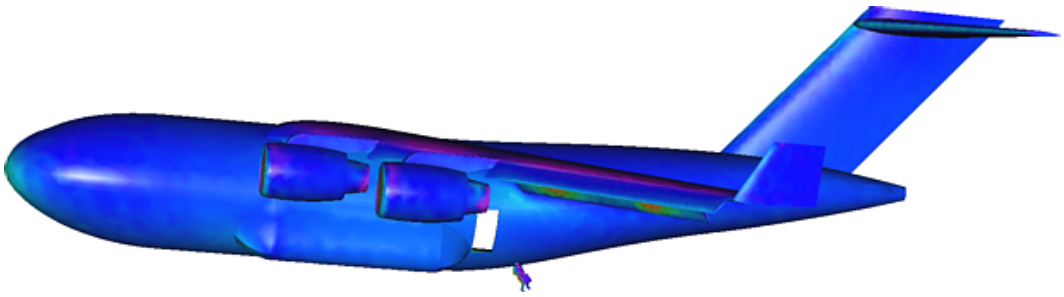

Figure 2. Aerodynamics of a paratrooper separating from an aircraft. Paratrooper separation from the aircraft. The colors on the paratrooper and aircraft surface show the air pressure distribution.

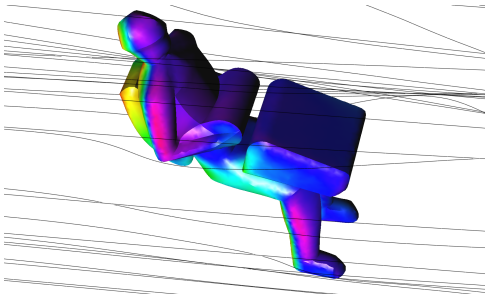

Figure 3. Aerodynamics of a paratrooper separating from an aircraft. Flow around the paratrooper. The streamlines and the air pressure distribution on the paratrooper.

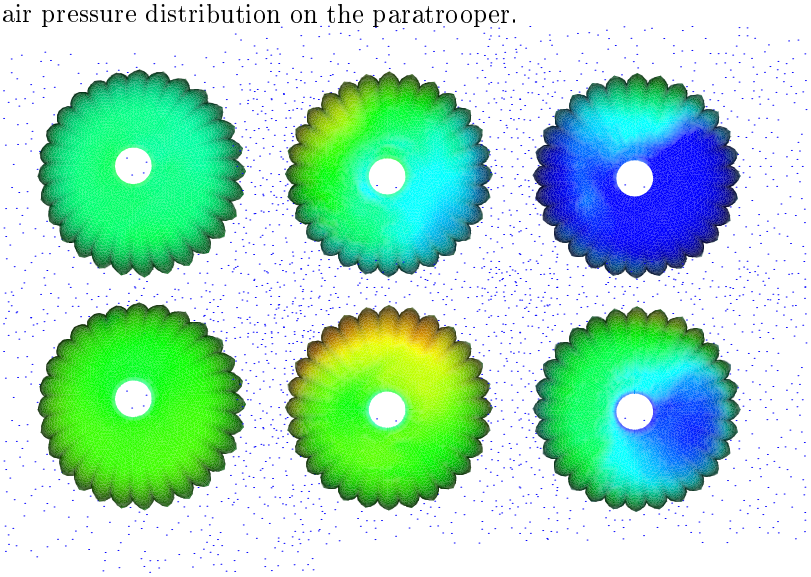

Figure 7. Fluid-structure interactions of a parachute crossing the far wake of an aircraft. Pressure distribution on the parachute canopy surface. Parachute in uniform flow (left), and in the wake at $t = 0.49$ (middle) and $t = 0.62$ (right). The upper and lower canopy surfaces are shown, respectively, in the upper and lower rows of pictures.

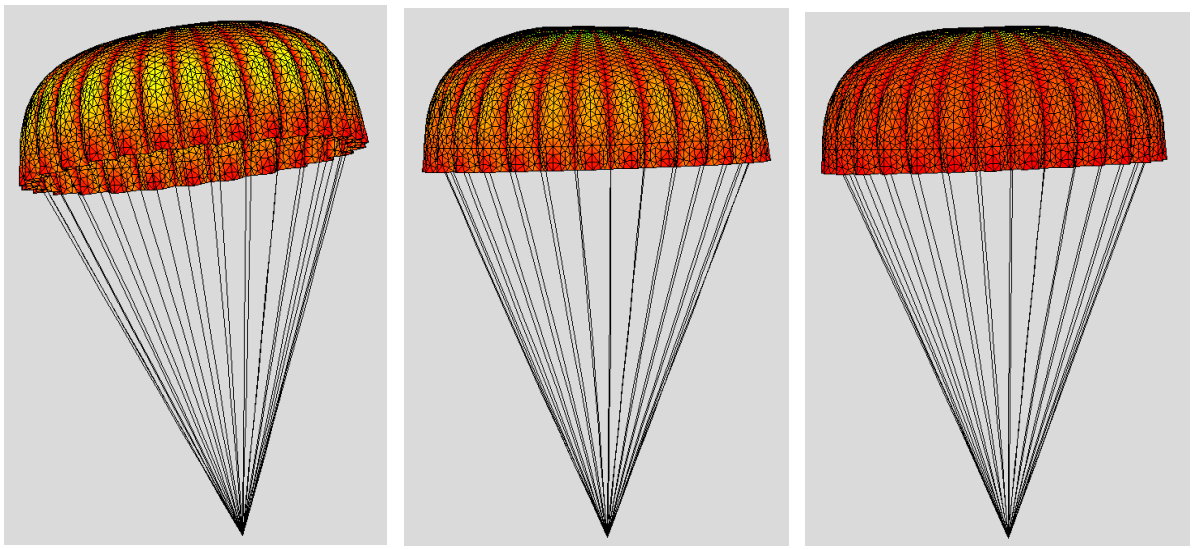

Figure 9. Fluid-structure interactions of a parachute crossing the far wake of an aircraft. Maximum principal stress for the parachute canopy. Parachute in uniform flow (left), and in the wake at $t = 0.49$ (middle) and $t = 0.62$ (right).

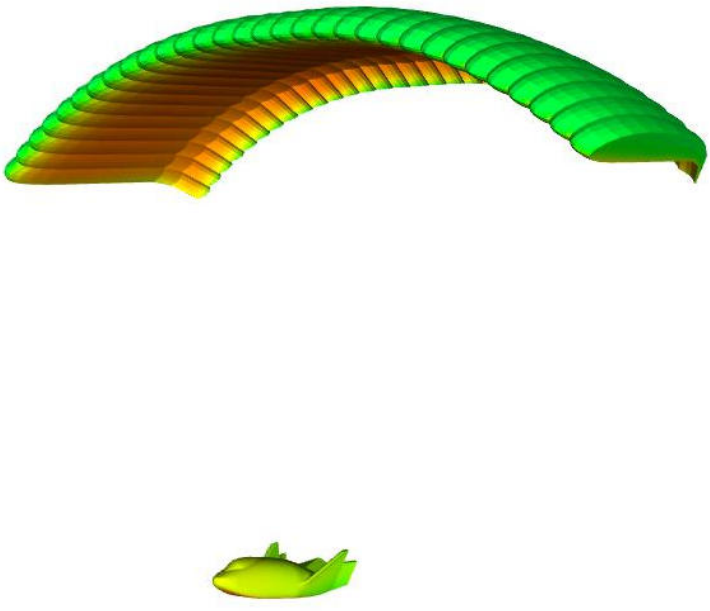

Figure 15. Aerodynamics of the Crew Return Vehicle and parafoil at different opening stages. Air pressure distribution on the surface of the CRV and parafoil for the final stage.